

An Efficient Learning Control Framework With Sim-to-Real for String-Type Artificial Muscle-Driven Robotic Systems

Jiyue Tao, Yunsong Zhang, Sunil Kumar Rajendran, Feitian Zhang*, Dexin Zhao, and Tongsheng Shen*

Abstract—Robotic systems driven by artificial muscles present unique challenges due to the nonlinear dynamics of actuators and the complex designs of mechanical structures. Traditional model-based controllers often struggle to achieve desired control performance in such systems. Deep reinforcement learning (DRL), a trending machine learning technique widely adopted in robot control, offers a promising alternative. However, integrating DRL into these robotic systems faces significant challenges, including the requirement for large amounts of training data and the inevitable sim-to-real gap when deployed to real-world robots. This paper proposes an efficient reinforcement learning control framework with sim-to-real transfer to address these challenges. Bootstrap and augmentation enhancements are designed to improve the data efficiency of baseline DRL algorithms, while a sim-to-real transfer technique, namely randomization of muscle dynamics, is adopted to bridge the gap between simulation and real-world deployment. Extensive experiments and ablation studies are conducted utilizing two string-type artificial muscle-driven robotic systems including a two degree-of-freedom robotic eye and a parallel robotic wrist, the results of which demonstrate the effectiveness of the proposed learning control strategy.

Index Terms—Machine learning for robot control, artificial muscle, deep reinforcement learning, sim-to-real.

I. INTRODUCTION

ARTIFICIAL muscles, designed to mimic biological counterparts, generate mechanical forces and movements in response to external stimuli like electrical or chemical signals. Well known for their high power-to-weight ratios and inherent compliance [1], artificial muscles offer a unique combination of strength and flexibility conducive to versatile and adaptive robot designs. Over the past decade, robotic systems driven by artificial muscles have achieved significant advancements, demonstrating impressive performance across diverse domains, including biomimetic robots [2]–[4], robot

manipulators and grippers [5], [6], soft robots [7], [8], and many others [9]–[11].

Despite their potential, achieving accurate control of string-type artificial muscle-driven robots remains a challenge due to their highly nonlinear and complex dynamics. While previous research efforts have primarily centered around structural design and open-loop motion performance evaluation [12]–[14], recent studies have begun to investigate closed-loop control strategies with a majority exploring proportional-integral-derivative (PID) controllers [15]–[17]. However, PID controllers often fall short in consistently delivering desired control performance, especially in complex robotic systems.

With the rapid development of machine learning techniques, learning-based controllers have emerged as an increasingly popular avenue in the muscle-driven robotics community. For instance, N. Nikdel *et al.* [6] developed a neural network-based model predictive controller for robotic manipulators actuated by shape memory alloys (SMAs). M. Giorelli *et al.* [18] established the inverse kinematics of cable-driven soft robotic arms using feedforward neural networks. T. Yang *et al.* [19] proposed a reinforcement learning control strategy for a cuttlefish-like soft robot driven by dielectric elastomer (DE) membranes. Among these approaches, deep reinforcement learning (DRL) stands out for its remarkable performance across diverse and complex tasks, offering a universal control solution. An increasing number of researchers have leveraged DRL algorithms to address control challenges in artificial muscle-driven robots, spanning applications ranging from dexterous grasping of robotic hands [20] to agile motion control of soft robotic manipulators [21], [22], and various others [23]–[26].

In most of existing studies [20], [22]–[24], [26], the standard procedure of applying DRL control in the targeted robotic systems typically follows the schematic illustrated in Fig. 1. Initially, it is crucial to identify the relevant parameters of the artificial muscles and formulate the system dynamics model to establish a simulation environment. Subsequently, the DRL algorithms undergo training within simulation to develop a control policy. Finally, the acquired control policy is deployed on the robotic platform to accomplish various control objectives. Despite these advancements, challenges persist in the application of DRL control in the targeted robotic systems.

1) *Muscle Sim-to-real Gap*: For the robotic systems driven by artificial muscles, modeling errors primarily come from the following three aspects. First, the dynamic models of

This work was partially supported by the National Key Research and Development Program of China under Grant 2022YFB4701900.

Jiyue Tao and Yunsong Zhang are with the Department of Advanced Manufacturing and Robotics, College of Engineering, Peking University, Beijing 100871, China. Jiyue Tao is also with the National Innovation Institute of Defense Technology, Beijing 100071, China (email: jiyuetao@pku.edu.cn; email: zysl1017@163.com).

Sunil Kumar Rajendran is with the BSS Technologies Inc., Takoma Park, MD 20912, USA (email: srajend2@gmu.edu).

Feitian Zhang is with the Department of Advanced Manufacturing and Robotics, and the State Key Laboratory of Turbulence and Complex Systems, College of Engineering, Peking University, Beijing 100871, China (email: feitian@pku.edu.cn).

Dexin Zhao and Tongsheng Shen are with the National Innovation Institute of Defense Technology, Beijing 100071, China (email: shents_bj@126.com; email: zhaodx2008@163.com).

*Send all correspondence to Feitian Zhang and Tongsheng Shen.

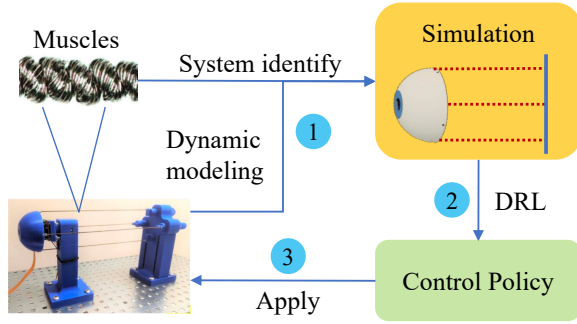


Fig. 1. Schematic of standard procedure of applying DRL control in artificial muscle-driven robotic systems. Three main steps include 1) dynamic modeling with system identification to establish simulation environment; 2) training DRL agent within the environment to develop a control policy; and 3) deploying the trained policy onto real-world robotic systems for testing.

artificial muscles themselves are approximate and inaccurate [27], [28]. Second, inevitable errors occur in the system identification process of the muscles. Third, different muscle strings typically have different model parameters [29], [30], and conducting system identification for all muscle strings is time-consuming and labor-intensive. These factors jointly contribute to inaccurate modeling of artificial muscles, resulting in a significant sim-to-real gap for the entire robotic system. Consequently, control strategies that perform well in simulation may not seamlessly transfer to real-world applications [21], [22]. Despite being labor-intensive, some researchers [19], [25] have attempted to directly train DRL algorithms on real robots. However, given the fragile nature of string-type artificial muscles [1], this approach lacks universality and safety guarantees. Hence, addressing the muscle sim-to-real gap for DRL-based controllers is imperative.

2) *Low Learning Efficiency*: In reinforcement learning, an agent continually interacts with the environment to acquire a good policy through learning from the interaction data [31]. Due to the complexity and high-dimensional nature of deep neural networks, DRL algorithms usually require a large amount of training data and iterations for convergence towards the desired policy. While training in simulation remains feasible, many studies have noted that the low sample efficiency often leads to significantly prolonged training times [23], [26], [32]. Moreover, the complex dynamic models of muscle-driven robots exacerbate this issue. Thus, enhancing training data efficiency and accelerating convergence speed are of great importance.

We observe a scarcity of research addressing the aforementioned issues within the domain of artificial muscle-driven robots. Our prior research [24] aimed to tackle the challenge of low learning efficiency. However, its experimental findings were solely derived from simulations, without addressing the crucial muscle sim-to-real gap. This paper presents a DRL-based control strategy with improved data efficiency and transferability to real-world applications. It is worth noting that in recent years, there have been some efforts to bridge the sim-to-real gap of artificial muscles. Many researchers [27], [28], [33]–[35] have proposed more accurate yet significantly more complex dynamic models. In this paper, however, we seek to

directly improve the performance of DRL-based controllers by employing a straightforward sim-to-real transfer technique, thereby bypassing the complicated process of mathematical modeling and parameter identification for artificial muscle strings. We evaluate our learning control framework on two robotic systems powered by artificial muscle strings, including a biomimetic robotic eye driven by super-coiled polymers (SCPs) [29], [36], and a parallel robotic wrist actuated by twisted-coiled actuators (TCAs) [30], [37].

The main contributions of this paper are as follows. To the best of our knowledge, this paper proposes the first efficient learning control framework designed for string-type artificial muscle-driven robotic systems. Specifically, we introduce a novel augmentation method for state-based data, which transforms a single transition data into several. We leverage an easy-to-implement PID controller to generate trajectories for early-stage training of DRL agents. The training results in simulation show that our proposed methods improve the data efficiency of the DRL algorithm in targeted robotic systems. Additionally, we leverage a zero-shot sim-to-real transfer technique on artificial muscle dynamics. The experimental results demonstrate a great improvement in real-world control performance through the application of this method in muscle-driven robotic systems. We believe that the proposed learning control framework can be utilized to address a variety of control tasks across similar robotic systems.

The remainder of this paper is organized as follows. Section II presents basic information about leveraging reinforcement learning within the robotic systems of interest. Section III offers a concise overview of the robotic platforms utilized in this study. Section IV presents our proposed efficient learning control framework in detail. Subsequently, Section V presents the experimental results of the proposed method, encompassing training outcomes in simulation and control performances in real-world scenarios. Finally, concluding remarks and current limitations are provided in Section VI.

II. PRELIMINARIES

In this section, we model the control problem of targeted robotic systems as a reinforcement learning problem by Markov Decision Process (MDP), which is a mathematical framework that describes the interaction between the DRL agent and the environment [31]. The MDP in artificial muscle-driven robots consists of the following tuple, i.e.,

$$(\mathcal{S}, \mathcal{A}, \mathcal{R}, f, \gamma). \quad (1)$$

- \mathcal{S} is the *state space*. At each time step t , the state vector $s_t \in \mathcal{S}$ generally includes the current state variables of the robotic system and the target positions and/or orientations. In this paper, the motion state variables of the robotic systems are collectively defined as vector \mathbf{x} , which contains the Euler angles, angular velocities, and other relevant motion states. The system output vector, containing the variables to be controlled, is denoted by \mathbf{y} . Correspondingly, the target system output is denoted by \mathbf{y}^* . In this way, the state vector s_t is represented as

$$s_t = (\mathbf{x}_t, \mathbf{y}^*). \quad (2)$$

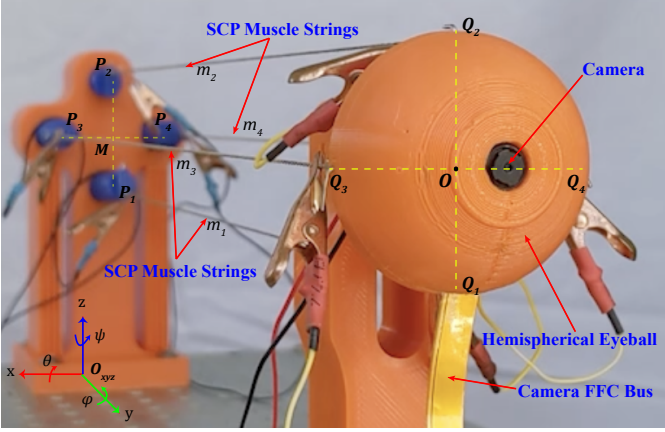


Fig. 2. The 2-DOF robotic eye prototype driven by two pairs of SCP muscles.

- \mathcal{A} is the *action space*, where each action $a_t \in \mathcal{A}$ is generated by the DRL agent based on the current state s_t and its own policy. The action vector typically consists of the actuating voltage applied to each muscle or the voltage difference between a pair of antagonistic muscles.
- \mathcal{R} is the *reward function* that maps the current state s_t and action a_t to an immediate reward r_t , i.e.,

$$r_t = \mathcal{R}(s_t, a_t). \quad (3)$$

The design of reward function plays a vital role in the learning process of the DRL agents, which learn the optimal policy under the guidance thereby. In this paper, we develop a generalized quadratic-form reward function design for the robotic systems of interest:

$$r_t = -(e_t^T Q_e e_t + a_t^T R_a a_t) + r_{\text{bonus}} \quad (4)$$

where $e_t = |\mathbf{y}^* - \mathbf{y}_t|$ is the system tracking error, and Q_e and R_a represent the output and control weight matrices, respectively. A bonus reward r_{bonus} is given when the system tracking error achieves a sufficiently small threshold. We add this bonus reward because, for the robotic systems discussed in this paper, maintaining at the target state is generally more challenging than reaching it.

- f represents the state transition function, which describes the likelihood of a transition from state s to s' when an action a is taken.
- $\gamma \in [0, 1]$ is the *discount factor*, which serves to balance the influence of future rewards on the current state. In all experiments conducted in this paper, we set γ to a constant value of $\gamma = 0.99$.

III. EXPERIMENTAL PLATFORMS

This section gives a concise overview of the testing platforms utilized in this paper, including an SCP-driven robotic eye (see Fig. 2) and a TCA-driven parallel robotic wrist (see Fig. 3). We briefly describe the hardware design, state space, action space, and reward function for each system.

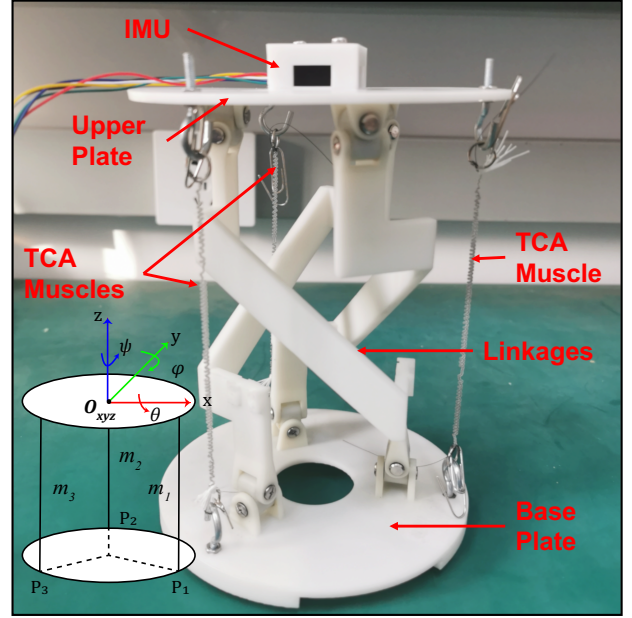


Fig. 3. The parallel robotic wrist prototype actuated by three TCAs.

A. Robotic Eye

The high occurrence of unsuccessful corrective surgeries for ocular motor disorders underscores the need for a muscle-driven robotic eye platform to assist ophthalmologists in gaining deeper insights into the biomechanics of human eye movement. In our previous work [36], we proposed a prototype of a 2-DOF robotic eye, and derived the geometric and dynamic models specific to this prototype. As illustrated in Fig. 2, the hemispherical eyeball is driven by two pairs of SCP muscle actuators, accommodating a Raspberry Pi Mini Camera (RPiMC). The primary control objective is to precisely and rapidly adjust the eyeball's orientation towards the desired target angles by regulating the SCP muscles, namely foveation control in the eye movement study.

The eyeball's center of rotation, denoted as $\mathbf{O} \in \mathbb{R}^3$, remains fixed at the origin within the reference frame O_{xyz} . Here, the axes x , y , and z correspond to the transverse, sagittal, and vertical axes of the eyeball, respectively. Rotations around these axes are expressed as pitch θ , roll ϕ , and yaw ψ . The robotic eye system's state variables are represented as

$$\mathbf{x} = [\theta, \dot{\theta}, \psi, \dot{\psi}, \Delta T_1, \Delta T_2, \Delta T_3, \Delta T_4] \quad (5)$$

where $\theta, \dot{\theta}, \psi, \dot{\psi}$ represent the pitch, yaw angles, and their respective angular velocities for control. Additionally, ΔT_i represents the temperature difference between the ambient temperature T_0 and the current temperature T_i of muscle m_i .

Focusing primarily on the robotic eye's orientation, the system's output vector is denoted as $\mathbf{y} = [\psi, \dot{\psi}, \theta, \dot{\theta}]$. Due to the difficulty and poor accuracy of measuring the temperature of each muscle in real time, the state vector of the DRL agent is defined by

$$s_t = [\theta_t, \dot{\theta}_t, \psi_t, \dot{\psi}_t, \theta^*, \psi^*]. \quad (6)$$

Here, θ^* and ψ^* represent the target angles. The Euler angles and corresponding angular velocities are measured through visual feedback from the embedded RPiMC. The actuating voltage applied to muscle m_i is denoted as V_i . Given the antagonistic configuration of the muscle pairs, the control input is defined by a constrained action vector, i.e.,

$$\begin{aligned} a_t &= [-V_1 + V_2, -V_3 + V_4] \\ \text{s.t. } &V_1 \cdot V_2 = V_3 \cdot V_4 = 0 \\ &0 \leq V_i \leq 10 \end{aligned} \quad (7)$$

The constraint requires that only one muscle is activated at each time step in the pairs (m_1, m_2) and (m_3, m_4) . The reward function follows the structure of (4), where the output and control weight matrices are set to $Q_e = \text{diag}\{0.05, 0.25, 0.05, 0.25\}$ and $R_a = \text{diag}\{0.01, 0.01\}$, respectively. The bonus reward is granted when the tracking error is sufficiently small, given by

$$r_{\text{bonus}} = 2 \times (\mathbf{1}\{|\psi - \psi^*| < 0.3\} + \mathbf{1}\{|\theta - \theta^*| < 0.3\}). \quad (8)$$

Here, $\mathbf{1}\{\cdot\}$ denotes the binary indicator function that yields a value of 1 if the given condition holds true, and 0 otherwise.

B. Robotic Wrist

Research into artificial muscle-driven robotic wrist joints holds considerable importance in several domains, including the development of dexterous robotic systems with human-like capabilities, advancements in rehabilitation and prosthetics technology, and the enhancement of robotic manipulation versatility across various fields. We designed a parallel robotic wrist prototype driven by three equally spaced compound TCAs [30] as illustrated in Fig. 3. The base plate remains stationary, while the upper plate, also known as the end effector, moves via three muscle strings. Linkages between the two plates are constructed to support two degree-of-freedom

motion of the upper plate [38]. Given this configuration, we developed a simplified dynamics model under the assumption of a fixed rotational center for the upper plate. Similar to the foveation control of the robotic eye, the control objective entails precise regulation of the moving upper plate's orientation. This necessitates adjusting the applied actuating voltages across the three muscle strings to drive the upper plate from its initial equilibrium state to predefined target angles.

The reference frame O_{xyz} is fixed on the moving upper plate, with the z -axis perpendicular to the upper plate and pointing outward. θ, ϕ , and ψ represent the pitch, roll, and yaw angles, respectively. Similar to the robotic eye, the system state variables are defined as

$$\mathbf{x} = [\theta, \dot{\theta}, \phi, \dot{\phi}, \Delta T_1, \Delta T_2, \Delta T_3] \quad (9)$$

where $\dot{\theta}$ and $\dot{\phi}$ represent the corresponding angular velocities, and ΔT_i is the temperature difference of muscle m_i with respect to the ambient environment, with $i \in \{1, 2, 3\}$. The system output vector is represented as $\mathbf{y} = [\theta, \dot{\theta}, \phi, \dot{\phi}]$. Likewise, the muscle's temperature is not used as an input for the DRL agent, and thus, the state vector is defined as

$$\mathbf{s}_t = [\theta_t, \dot{\theta}_t, \phi_t, \dot{\phi}_t, \theta^*, \phi^*]. \quad (10)$$

Here, θ^* and ϕ^* denote the target angles, with the respective Euler angles and angular velocities measured using the inertial measurement unit (IMU) positioned at the center of the upper plate. Additionally, the input action vector a_t of the system is defined as

$$a_t = [V_1, V_2, V_3] \quad (11)$$

where V_i represents the actuating voltage applied to muscle m_i , constrained by $0 \leq V_i \leq 10$. The output and control weight matrices of the reward function are set to $Q_e = \text{diag}\{0.05, 0.2, 0.05, 0.2\}$ and $R_a = \text{diag}\{0.01, 0.01\}$,

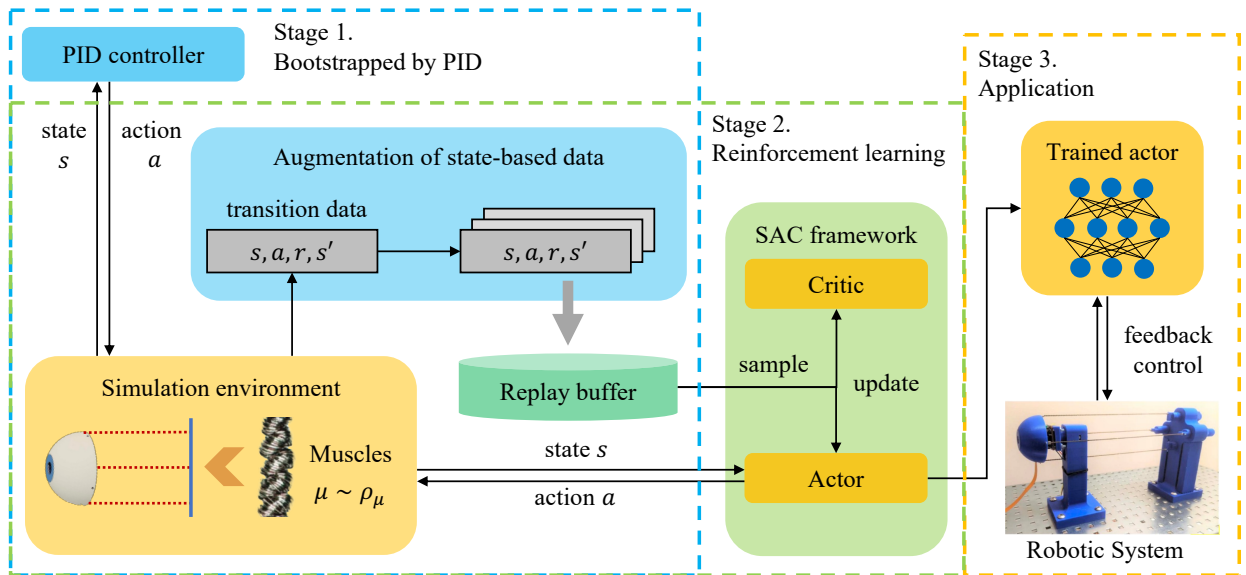


Fig. 4. Overview of the proposed efficient learning control framework, including a two-stage training process in simulation and real-world application. Stage 1 utilizes bootstrapping with PID control, aiming at enhancing data efficiency. Stage 2 integrates the baseline SAC learning algorithm with state-based data augmentation and randomization of muscle dynamics for expediting training convergence and bridging sim-to-real gap, respectively.

respectively. When the tracking error is sufficiently small, a bonus reward is granted, i.e.,

$$r_{\text{bonus}} = 2 \times (\mathbb{1}\{|\theta - \theta^*| < 0.5\} + \mathbb{1}\{|\phi - \phi^*| < 0.5\}). \quad (12)$$

IV. LEARNING CONTROL FRAMEWORK

This section provides a comprehensive overview of the proposed learning control framework, as illustrated in Fig. 4. The soft actor-critic (SAC) serves as the baseline DRL algorithm. To enhance data efficiency, we employ a two-stage training strategy. Initially, a standard PID controller is initialized to generate imperfect trajectories for the DRL agent. Subsequently, the agent interacts directly with the simulation environment to update its policy. All transition data observed from the environment undergoes a state-based augmentation strategy before being stored into the replay buffer. To address the sim-to-real gap, we introduce a randomization method on the artificial muscle dynamics at the beginning of each training episode. Eventually, the trained actors (control policies) are able to be directly applied in real-world robotic systems to achieve desired control performance.

A. Soft Actor-Critic (SAC)

SAC, a state-of-the-art deep reinforcement learning algorithm, finds extensive application across various tasks [39]. Traditional DRL algorithms primarily maximize cumulative rewards, i.e.,

$$J(\pi) = \sum_{t=0}^T \mathbb{E}_{(s_t, a_t) \sim \rho_\pi} [\mathcal{R}(s_t, a_t)] \quad (13)$$

where π represents the policy. However, SAC adopts an entropy-maximizing approach, with its learning objective formulated as

$$J(\pi) = \sum_{t=0}^T \mathbb{E}_{(s_t, a_t) \sim \rho_\pi} [\mathcal{R}(s_t, a_t) + \alpha \mathcal{H}(\pi(\cdot|s_t))]. \quad (14)$$

where $\mathcal{H}(\pi(\cdot|s_t))$ represents an entropy of the policy π , and α serves as a temperature parameter. This approach enhances the robustness of DRL and accelerates its training process [31].

In addition, SAC is an off-policy algorithm that leverages the actor-critic architecture. The neural network structures utilized in this paper are illustrated in Fig. 5. To process the sequential information crucial for implementing dynamics randomization and handling partial observability, we employ a Gated Recurrent Unit (GRU) [40]. We select GRU over over commonly-used Long Short-Term Memory (LSTM) due to its efficiency and ease of training [40]. Noise is added to the observation input to the actor. The hyperparameters of the SAC algorithm are detailed in Table I and remain consistent across all ablation studies conducted in this paper.

B. Randomization of Muscle Dynamics

The core idea behind dynamics randomization is to introduce randomness into specific dynamic parameters within the simulator during training. This approach allows the DRL agent to learn a policy adaptable to various dynamics conditions,

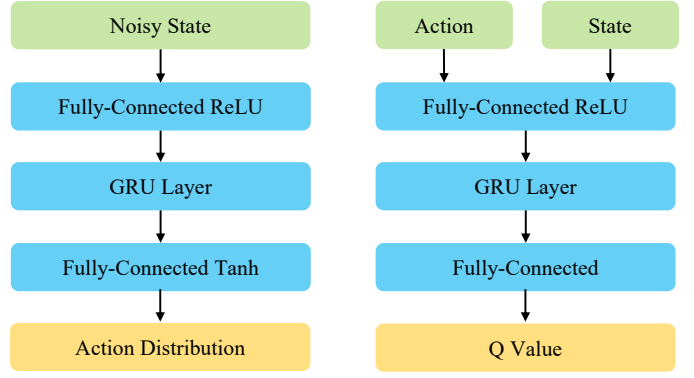


Fig. 5. Schematic diagram of the network architecture. The actor (left) and the critic (right) networks share the same structure but have different parameters. Each is composed of a fully-connected layer with ReLU activation as the input layer, a recurrent GRU [40] unit, and a fully-connected output layer.

TABLE I
SAC HYPER-PARAMETERS

Parameter	Value
Learning rate of actor	1×10^{-4}
Learning rate of critic	1×10^{-4}
Replay buffer size	1×10^5
Mini-batch size	20
Entropy target	$-\dim(\mathcal{A})$ (e.g., -3 for robotic wrist)
Soft update factor τ	0.005
Discount factor γ	0.99
Hidden layer size of GRU	256
Gradient steps k	40
Target networks update interval	1

including those encountered in real-world experiments. Widely adopted in diverse robotic applications [41]–[43], this method serves as inspiration for our work. Specifically, we randomize several critical parameters within the simulated dynamics environment. Among the robotic systems discussed in this paper, the dynamic parameter set of the muscles, denoted by μ , holds pivotal importance. Therefore, we establish a distribution ρ_μ to encompass the variability of muscle dynamic parameters for dynamics randomization purposes. Additionally, we incorporate Gaussian noise into the observation inputs of the policy to emulate the noise commonly present in real-world sensor data.

Regarding the SCP muscles driving the robotic eye and the TCA muscles driving the parallel robotic wrist, their thermomechanical models are approximately as [29]

$$F = k(x - x_0) + b\dot{x} + c(T(t) - T_{\text{amb}}). \quad (15)$$

Here, x and x_0 represent the loaded length and unloaded length of the actuator, respectively. k , b , and c denote the mean stiffness, damping, and temperature effect of the actuator, respectively. $T(t)$ denotes the current temperature, while T_{amb} stands for the ambient temperature of the environment. The thermoelectric model of the actuator is expressed as

$$C_{\text{th}} \frac{dT(t)}{dt} = P(t) - \lambda(T(t) - T_{\text{amb}}). \quad (16)$$

TABLE II
DYNAMICS PARAMETERS OF RANDOMIZATION AND THEIR RESPECTIVE RANGE IN THE ROBOTIC EYE

Parameter	Value	Scaling factor	Additive term
k (N/cm)	0.25	uniform(0.8, 1.2)	-
b ($N \cdot s/cm$)	0.01	uniform(0.9, 1.1)	-
c ($N/^\circ C$)	0.0055	uniform(0.85, 1.15)	-
C_{th} ($Ws/^\circ C$)	0.28	uniform(0.8, 1.2)	-
λ ($W/^\circ C$)	0.094	uniform(0.85, 1.15)	-
R (Ω)	20.0	uniform(0.9, 1.1)	-
θ, ψ noise ($^\circ$)	-	-	normal(0, 0.1)
$\dot{\theta}, \dot{\psi}$ noise ($^\circ/s$)	-	-	normal(0, 0.05)

Here, C_{th} represents the thermal mass of the actuator, and λ represents the absolute thermal conductivity of the actuator. $P(t)$ stands for the heat power applied to the actuator, calculated as $P(t) = V^2/R$, where V is the voltage applied to the actuator and R is the electrical resistance. In summary, the dynamic parameter set for randomization is

$$\mu := \{k, b, c, C_{th}, \lambda, R\} \quad (17)$$

Table II and III outline the distribution ρ_μ of SCP and TCA muscles, respectively, along with the observation noise added for the robotic eye and wrist systems. ρ_μ is centered on the mean values derived from system identification to align the data distribution in simulation more accurately with that in reality. The range of randomization for each parameter is determined based on the distribution observed across different real muscle strings, as outlined in previous work [29]. During the training process, the physical parameters of the actuators are randomized within the scaling ranges (i.e., $\mu \sim \rho_\mu$) at the beginning of each training episode and remain constant throughout. Whereas, the observation noise varies at each time step and across different Euler angles. While this paper employs a simplified linear dynamic model for artificial muscles, this method is expected to be readily transferred to more complex muscle dynamics models.

C. Bootstrap via PID

On-line DRL agents mainly rely on random exploration [31]. However, due to the slow response of artificial muscles, random exploration policies may struggle to explore the state space comprehensively and rapidly, resulting in low sample efficiency. To address this issue, we draw inspiration from previous work [44], [45] and boost the training process by providing demonstrations into initial replay buffer. While PID controllers demand extensive tuning for optimal control performance, their implementation is relatively straightforward, given that moderate performance suffices. In the case of muscle-driven robotic systems, PID policies typically suffice to approach the target state. Hence, they provide trajectories that explore the defined state space more comprehensively, serving as an advantageous starting point for the DRL learning process. Subsequently, the agent will interact with the environment and continue to refine its policy, thus eventually outperforming PID and achieving desired control performances.

Before the DRL training process begins, we initialize a PID controller that offers a barely acceptable (and typically not

TABLE III
DYNAMICS PARAMETERS OF RANDOMIZATION AND THEIR RESPECTIVE RANGE IN THE ROBOTIC WRIST

Parameter	Value	Scaling factor	Additive term
k (N/mm)	0.21	uniform(0.8, 1.2)	-
b ($N \cdot s/cm$)	0.63	uniform(0.9, 1.1)	-
c ($N/^\circ C$)	0.0707	uniform(0.85, 1.15)	-
C_{th} ($Ws/^\circ C$)	3.06	uniform(0.8, 1.2)	-
λ ($W/^\circ C$)	0.1189	uniform(0.85, 1.15)	-
R (Ω)	10.0	uniform(0.9, 1.1)	-
θ, ϕ noise ($^\circ$)	-	-	normal(0, 0.1)
$\dot{\theta}, \dot{\phi}$ noise ($^\circ/s$)	-	-	normal(0, 0.05)

excellent) control performance. Within the first M episodes of training, the PID controller interacts with the environment and generates trajectories, which are then stored in the replay buffer along with the the rewards. Differing from traditional behavior cloning methods, we don't utilize a supervised loss during demonstration learning. Consequently, the agent does not strictly follow the PID control policy but leverages the trajectories generated by PID solely to bootstrap the initial training.

D. Augmentation of State Vector

Data augmentation refers to a class of techniques aimed at enhancing the size and quality of training datasets, thereby facilitating the development of more robust deep learning models [46]. The fundamental concept of data augmentation involves transforming limited data into diverse, functionally equivalent datasets. Given the labor-intensive and computationally expensive nature of collecting training data in robotic systems, we integrate data augmentation into the agent's learning process. While prior research [47]–[49] has explored data augmentation in reinforcement learning, existing studies have primarily focused on pixel-based RL scenarios, where agents rely on image-based observations. In this paper, we present a straightforward and adaptable approach to state-based data augmentation, better suited and more effective for our targeted robotic systems.

As commonly acknowledged, rewards serve as pivotal guides in the learning process of DRL agents. Therefore, our objective is to generate more data transitions with different rewards. By combining (2) and (3), the reward r_t is then calculated as

$$r_t = \mathcal{R}(\mathbf{x}_t, \mathbf{y}^*, a_t). \quad (18)$$

Here, \mathbf{x}_t and a_t are directly related to system dynamics, whereas the target output vector \mathbf{y}^* is manually set and changeable. Consequently, the proposed augmentation of state vector proceeds as follows. At each time step t , we fix the motion state vectors $\mathbf{x}_t, \mathbf{x}_{t+1}$ and the action a_t , and vary the target vector \mathbf{y}^* . In this paper, we introduce a random additive term into \mathbf{y}^* as follows

$$\mathbf{y}_{new}^* = \mathbf{y}^* \pm \delta \mathbf{Z}. \quad (19)$$

Here, \mathbf{y}_{new}^* denotes the new target vector. δ acts as a scalar factor to control the scope of augmentation, which largely depends on the defined range. \mathbf{Z} is a random vector sharing

Algorithm 1 Augmentation of State-based Data

```

1: Generate rollout  $\tau = (s_0, a_0, r_0, \dots, s_T)$  from environment
2: for  $i = 1$  to  $n$  do
3:   for each  $s_t, a_t, r_t$  in  $\tau$  do
4:     Create a new state vector  $s_t \rightarrow s'_t$ 
5:     Calculate a new reward  $r'_t = \mathcal{R}(s'_t, a_t)$ 
6:   end for
7:   Get a new rollout  $\tau'_i = (s'_0, a_0, r'_0, \dots, s_T)$ 
8: end for

```

TABLE IV
SIMULATION PARAMETERS OF ROBOTIC SYSTEMS

	Description	Symbol	Value
Robotic Eye	Total time duration of one episode	t_{total}	15s
	Action time step	t_a	0.5s
	Total number of training episodes	N	2000
	Random or boost episodes	M	250
	Absolute value of θ bound	θ_{max}	15°
	Absolute value of ψ bound	ψ_{max}	10°
Robotic Wrist	Total time duration of one episode	t_{total}	30s
	Action time step	t_a	0.5s
	Total number of training episodes	N	3500
	Random or boost episodes	M	500
	Absolute value of θ bound	θ_{max}	15°
	Absolute value of ϕ bound	ϕ_{max}	15°

identical dimensions with \mathbf{y}^* , wherein the elements of \mathbf{Z} range from 0 to 1. Thus, we derive a pair of new states s'_t and s'_{t+1} . After that, a new corresponding reward r'_t is calculated using (18). Following the above steps, the original transition tuple is transformed into a new one, i.e.,

$$(s_t, a_t, r_t, s_{t+1}) \xrightarrow{\text{AUG}} (s'_t, a_t, r'_t, s'_{t+1}). \quad (20)$$

The procedure of using augmentation for a state-based trajectory τ is provided in Algorithm 1. Each time the agent interacts with the environment and gets a new trajectory, this method creates n different trajectories at a very low computational cost. We set $n = 10$ in both robotic eye and wrist systems during training. In this paper, we denote the bootstrap method by the letter 'B', augmentation method by the letter 'A', and randomization of muscle dynamics by the letter 'R'. Algorithm 2 provides a detailed overview of the entire training procedure for the SAC algorithm with all three proposed improvements (i.e., SAC-BAR).

V. EXPERIMENTAL RESULTS

This section presents the experimental results of the proposed efficient learning control framework within two testing robotic platforms. We first present the training results of the algorithm in simulation environments, validating the effectiveness of the proposed bootstrap and augmentation methods in enhancing training data efficiency. Subsequently, we demonstrate the results of an ablation study conducted on the robotic wrist platform, verifying the effectiveness of dynamics randomization in improving the real-world control performance. Finally, experimental results on robotic eye are

Algorithm 2 SAC-BAR Learning Control

```

1: Initialize critic networks  $Q_{\theta_1}, Q_{\theta_2}$ , and actor network  $\pi_\phi$ 
   with random parameters  $\theta_1, \theta_2, \phi$ 
2: Initialize target network parameters  $\bar{\theta}_1 \leftarrow \theta_1, \bar{\theta}_2 \leftarrow \theta_2$ 
3: Initialize an empty replay buffer  $\mathcal{B}$ 
4: Initialize a PID controller  $\pi_{\text{PID}}$ 
5: Initialize dynamics parameters distribution  $\rho_\mu$ 
6: for step = 1 to  $M$  do
7:   Sample dynamics  $\mu \sim \rho_\mu$ 
8:   Generate rollout  $\tau_0 = (s_0, a_0, r_0, \dots, s_T)$  with dynamics
    $\mu$  and  $a_t \sim \pi_{\text{PID}}(s_t)$ 
9:   for  $i = 1$  to  $n$  do
10:    Create new rollouts  $\tau_0 \xrightarrow{\text{AUG}} \tau_i$ 
11:   end for
12:   Store  $\tau_0, \tau_1, \dots, \tau_n$  into  $\mathcal{B}$ 
13: end for
14:
15: for step =  $M + 1$  to  $N$  do
16:   Sample dynamics  $\mu \sim \rho_\mu$ 
17:   Generate rollout  $\tau_0 = (s_0, a_0, r_0, \dots, s_T)$  with dynamics
    $\mu$  and  $a_t \sim \pi_\phi(s_t)$ 
18:   for  $i = 1$  to  $n$  do
19:    Create new rollouts  $\tau_0 \xrightarrow{\text{AUG}} \tau_i$ 
20:   end for
21:   Store  $\tau_0, \tau_1, \dots, \tau_n$  into  $\mathcal{B}$ 
22:   for  $i = 1$  to  $k$  do
23:    Sample a mini-batch of rollouts from  $\mathcal{B}$ 
24:    Calculate the gradients  $\nabla J_Q(\theta_i), \nabla J_\pi(\phi), \nabla J(\alpha)$ 
25:    Update network weights:
26:     $\theta_i \leftarrow \theta_i - \lambda_Q \nabla J_Q(\theta_i)$ 
27:     $\phi \leftarrow \phi - \lambda_\pi \nabla J_\pi(\phi)$ 
28:     $\bar{\theta}_i \leftarrow \tau \theta_i + (1 - \tau) \bar{\theta}_i$ 
29:    Adjust temperature parameter:
30:     $\alpha \leftarrow \lambda_\alpha \nabla J(\alpha)$ 
31:   end for
32: end for

```

provided to demonstrate the generalizability of the proposed control framework across different robotic systems of interest.

A. Training Results

We established simulation environments for two robotic systems to train DRL agents and conduct preliminary tests. Table IV lists the simulation parameters for each robotic system. The overall duration of a single episode t_{total} and the action time step t_a depend on the rise time and response speed constraints inherent to the hardware of the systems. The values of N and M are empirical parameters contingent on the complexity of the systems. For simpler dynamics, smaller values for N and M facilitate the learning process for the DRL agent in acquiring an effective control policy. For algorithms not using the bootstrap method, random exploration is employed in the first N episodes. Target angles are confined within the motion range of the robotic device. With the majority of training time spent on dynamics calculation, the time step for dynamics simulation is set at 0.01s to balance

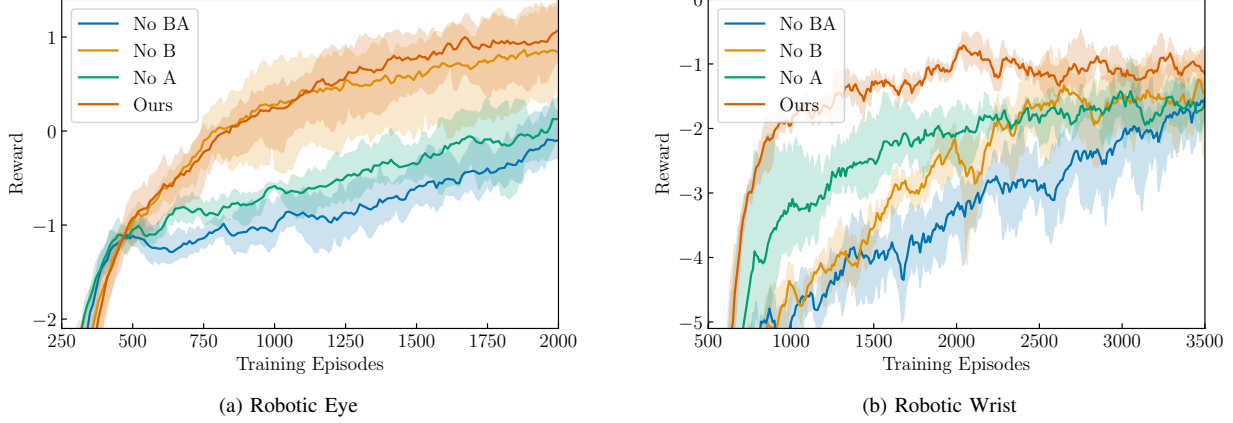


Fig. 6. Reward trajectories with respect to the training episode number in ablation study. Ours refers to the proposed SAC-BAR algorithm, where B, A, and R indicate bootstrap, augmentation, and randomization techniques, respectively. Performance is evaluated in simulation with random dynamics every 10 training episodes. The shaded area indicates the standard deviation of the mean reward based on running each experiment with three different random seeds.

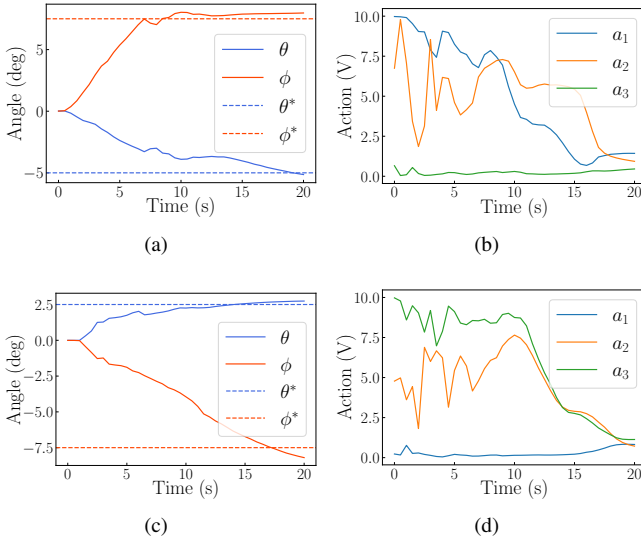


Fig. 7. Experimental trajectories of vanilla SAC algorithm on the robotic wrist under target angles ($\theta^* = -5^\circ, \phi^* = 7.5^\circ$) and ($\theta^* = 2.5^\circ, \phi^* = -7.5^\circ$), respectively. (a), (c) The system output angles (θ, ϕ). (b), (d) The corresponding actions a_t generated by the trained actor.

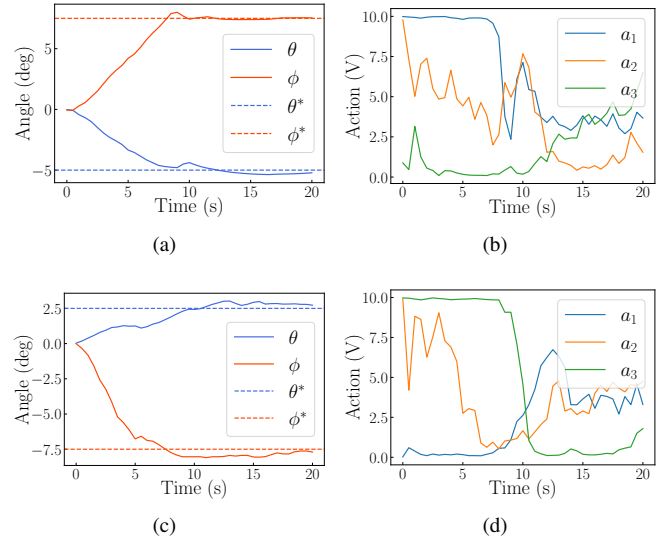


Fig. 8. Experimental trajectories of our proposed SAC-BAR algorithm on the robotic wrist under target angles ($\theta^* = -5^\circ, \phi^* = 7.5^\circ$) and ($\theta^* = 2.5^\circ, \phi^* = -7.5^\circ$), respectively. (a), (c) The system output angles (θ, ϕ). (b), (d) The corresponding actions a_t generated by the trained actor.

simulation accuracy and computational efficiency. Training and testing in simulation are conducted on a computer with an Intel Xeon Platinum 8383C CPU and an NVIDIA GeForce RTX 4090 GPU. The algorithms are implemented in PyTorch and trained using the Adam optimizer.

In each training episode, a target state is randomly selected from a uniformly distributed range. For instance, in the robotic eye scenario, the target angles adhere to $\theta^* \sim \mathcal{U}[-15^\circ, 15^\circ]$ and $\psi^* \sim \mathcal{U}[-10^\circ, 10^\circ]$. The robotic agent endeavors to reach the target from the initial state throughout the episode. For algorithms incorporating dynamics randomization, a new set of muscle dynamics parameters μ is sampled at the beginning of each episode by drawing values for each parameter from their respective range. Additionally, simulated sensor noise is introduced to the observed state at every action step. In the absence of dynamics randomization, muscle parameters are

kept constant at their mean values, and no simulated noise is added during the training process.

To evaluate the effectiveness of the proposed bootstrap and augmentation techniques, we conducted an ablation study on two robotic systems. Training results of our learning control design, with and without bootstrap and augmentation, are presented in Fig. 6. The policies were trained and evaluated in simulation with random dynamics. As illustrated in the figures, our proposed algorithm exhibits the highest level of data efficiency in both robotic systems. Compared to the SAC algorithm trained solely with dynamics randomization (referred to as "No BA"), the integration of bootstrap and augmentation enhances data efficiency and expedites the training process. In the robotic eye system, the baseline algorithm achieves an average reward of -0.10 after 2000 training episodes, whereas our approach achieves comparable performance in

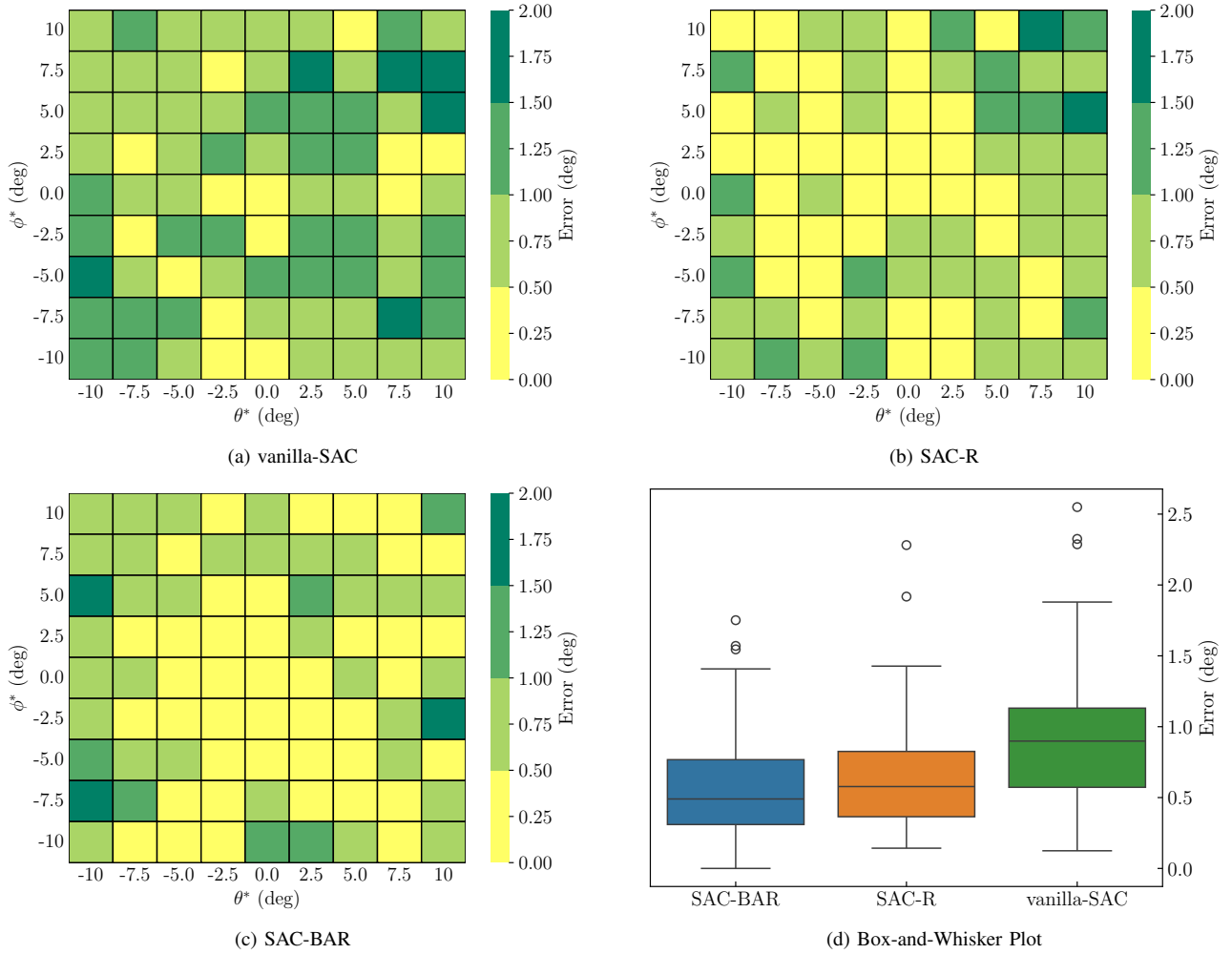


Fig. 9. Experimental results of the steady-state error tests in the parallel robotic wrist under selected control algorithms. (a), (b), (c) Heat maps illustrating the experimental results for the vanilla SAC algorithm, SAC with the randomization of muscles only (SAC-R), and our complete efficient learning control algorithm (SAC-BAR), respectively. The combination of target angles (θ^*, ϕ^*) is systematically spaced at 2.5° intervals within the range $(|\theta^*|, |\phi^*|) \leq 10^\circ$. The color bars in the visualization indicate the Euclidean distance norm of steady-state errors. (d) The box charts illustrating the medians, maxima, minima, quartiles, and outliers of the steady-state errors for the selected comparative control algorithms.

only approximately 750 episodes, resulting in a data efficiency increase to 2.67 times the original level. Similarly, in the robotic wrist system, the baseline algorithm achieves an average reward of -1.61 after 3500 episodes, while ours achieves comparable performance in only about 1200 episodes, leading to a data efficiency increase to 2.92 times. Notably, in the case of the more complex robotic wrist system, the demonstrations provided by the PID controller yield a more significant acceleration effect during the early stages of training. Meanwhile, the augmentation method demonstrates a favorable impact on enhancing the training speed in both systems.

B. Ablation Study in Robotic Wrist Experiments

To evaluate the impact of each component on real-world control performances, three different control policies are tested on the robotic wrist platform, including the vanilla SAC algorithm, SAC with only randomization of muscles (SAC-R), and our proposed efficient learning control framework (SAC-BAR). All three algorithms undergo training for an equivalent

TABLE V
AVERAGED STEADY-STATE ERROR OVER A TOTAL OF 81 TARGETS IN
ABLATION STUDY WITH THE ROBOTIC WRIST

Agent	Vanilla-SAC	SAC-R	SAC-BAR
Mean error (deg)	0.911 ± 0.457	0.657 ± 0.386	0.580 ± 0.368

number of episodes in simulation, employing identical hyperparameters as specified in Table IV. During each experimental episode, the parallel robotic wrist starts from the initial state with $\theta = \phi = 0^\circ$ and attempts to reach and maintain the target angle set (θ^*, ϕ^*) . The action vector a is computed by the trained actors at a time step of $t_a = 0.5s$, and each episode spans a duration of $t_{total} = 20s$. Observations are measured by an IMU positioned at the center of the upper plate.

The experimental trajectories for two pairs of desired target angles, $(\theta^*, \phi^*) = (-5^\circ, 7.5^\circ)$ and $(\theta^*, \phi^*) = (2.5^\circ, -7.5^\circ)$, of the vanilla SAC algorithm and our proposed SAC-BAR are illustrated in Fig. 7 and Fig. 8, respectively. In Fig. 7(a)

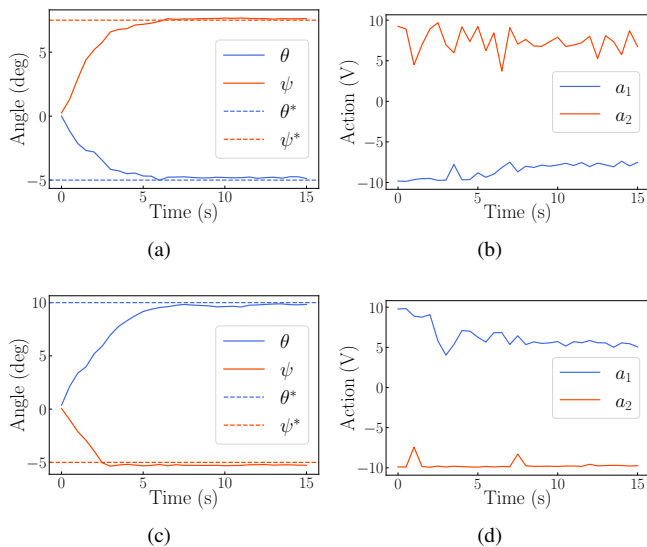


Fig. 10. Experimental trajectories of the foveation test of the 2-DOF robotic eye. Target angles are set at $(\theta^* = -5^\circ, \psi^* = 7.5^\circ)$ and $(\theta^* = 10^\circ, \psi^* = -5^\circ)$, respectively. (a), (c) The system output angles (θ, ψ) . (b), (d) The corresponding actions a_t generated by the trained actor.

and (c), it is evident that without randomization of muscle dynamics, the vanilla-SAC agent struggles to achieve the desired orientation. While the agent may eventually reach the desired orientation at certain target angles, maintaining that target angle becomes a challenge, resulting in a considerable steady-state error. Conversely, as observed in Fig. 8(a) and (c), the proposed SAC-BAR agent achieves the target state in less than 10s and consistently remains within its neighborhood thereafter. This success is attributed to the agent learning to maximize the action value during the rising phase and promptly reduce it upon approaching the target angles, as illustrated by the input action trajectories in Fig. 8(b) and (d). Additionally, when overshoot occurs, the agent still learns to return to and maintain the target orientation. Conversely, in Fig. 7(b) and (d), there exist serious oscillations in the action trajectories of vanilla SAC agent during the initial 10s, leading to a prolonged rise time and sometimes even failure to reach the target.

In order to comprehensively evaluate the control performance of the algorithms across different target angles, we design a steady-state error field test for the robotic wrist. We select a series of target angles (θ^*, ϕ^*) spaced at 2.5° intervals within the defined range $\theta^*, \phi^* \in [-10^\circ, 10^\circ]$. Each agent is set to run for 25s, sequentially targeting each angle pair. The steady-state error is measured and averaged over the last 5s window, determined by computing the Euclidean distance norm between the current and target angles using $e_{ss} = \sqrt{(\theta - \theta^*)^2 + (\phi - \phi^*)^2}$.

The steady-state errors of the field test of vanilla-SAC, SAC-R, and SAC-BAR are presented in Fig. 9(a), (b), and (c), respectively. The x and y axes therein represent θ^* and ϕ^* , while the color bars represent the averaged steady-state errors. Following that, box charts in Fig. 9(d) illustrate the medians, maxima, minima, quartiles, and outliers of the steady-state

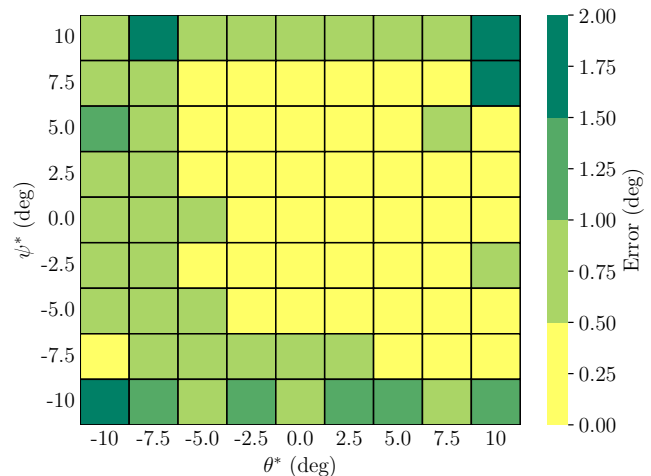


Fig. 11. Experimental results in the steady-state error tests of the robotic eye at every combination of (θ^*, ψ^*) target angles spaced at 2.5° intervals for $(|\theta^*|, |\psi^*|) \leq 10^\circ$ where the color bar represents the Euclidean distance norm of steady-state error.

errors for different control policies. The figures demonstrate that vanilla-SAC agent performs poorly across nearly the entire defined range, whereas both SAC-R and SAC-BAR outperform significantly. The steady-state errors averaged over the defined range for three algorithms are presented in Table V. Compared to the baseline vanilla-SAC, SAC-R and SAC-BAR achieved reductions in averaged steady-state errors of 27.9% and 36.3%, respectively. Specifically, our proposed SAC-BAR reaches the desired orientation at every target angle pair with steady-state errors consistently bounded below 1.5° except for three outliers. The averaged steady-state error of SAC-BAR is 0.58° , demonstrating its superior control performance in accuracy and robustness across different target angles.

The above experimental results indicate that randomization of muscle dynamics significantly enhances the real-world control performance of the learning-based controllers in the robotic system of interest, while bootstrap and augmentation techniques contribute less to the improvement. We believe that the enhancement observed in SAC-BAR compared to SAC-R primarily stems from the improvement in training efficiency. With the incorporation of bootstrap and augmentation methods, SAC-BAR achieves more comprehensive training and higher averaged rewards in simulation after 3500 training episodes. This improvement is potentially more significant in scenarios where training data is limited or exploration proves more challenging.

C. Learning Control of Robotic Eye

To demonstrate the applicability of the proposed learning control framework across diverse robotic systems driven by artificial muscle strings, this subsection presents experimental results on an additional platform, the 2-DOF robotic eye. We focus on the foveation control in the experiment. The robotic eye system, initialized at $\theta = \psi = 0^\circ$ in ambient room temperature, is configured to foveate at various target angles (θ^*, ψ^*) . Considering the system's rise time, each testing episode lasts

for $t_{\text{total}} = 15\text{s}$, with an action time step of $t_a = 0.5\text{s}$. The averaged Euclidean distance between the current and target angles within the last 5s window serves as the steady-state error metric, i.e., $e_{\text{ss}} = \sqrt{(\theta - \theta^*)^2 + (\psi - \psi^*)^2}$.

Experimental trajectories with targets set at $(\theta^*, \psi^*) = (-5^\circ, 7.5^\circ)$ and $(10^\circ, -5^\circ)$ are illustrated in Fig 10. These trajectories demonstrate that the measured angles rise to the target in approximately 5s , with negligible steady-state error. A visual field test is conducted with a series of target angles spaced at 2.5° intervals within the defined range $|\theta^*|, |\psi^*| \leq 10^\circ$ to evaluate the overall control performance of the algorithm. The robotic eye is tested to foveate at each target in sequence. The results, illustrated in Fig. 11, reveal excellent control performance, with steady-state errors consistently below 1° for most target angles.

In prior research [23], we adopted a reinforcement learning-based controller using deep deterministic policy gradient (DDPG) algorithm [50], trained in simulation for 50000 episodes. Additionally, a reduced-order state observer estimated the real-time temperature of SCP muscles, resulting in satisfactory control performance. In this paper, our proposed algorithm demonstrates comparable control performance with just 2000 training episodes, representing only $1/25$ of the original requirement. Remarkably, it accomplishes this without the need for real-time muscle temperature information.

VI. CONCLUSIONS

This paper presented a learning-based control framework designed for the string-type artificial muscle-driven robotic systems, leveraging the SAC algorithm with a GRU hidden layer as the baseline DRL algorithm. To enhance training data efficiency and expedite convergence speed, we proposed two methods including bootstrap by PID and state-based data augmentation. Additionally, we incorporated randomization of artificial muscle dynamic parameters during training to address the sim-to-real gap for enhancing real-world control performance. Extensive experiments and ablation studies on two systems—a 2-DOF robotic eye driven by SCP actuators and a parallel robotic wrist driven by TCA muscles—validated the effectiveness and generalizability of the proposed control framework.

In simulation, the designed bootstrap and augmentation methods significantly reduced the training episodes required for DRL-based controllers. Real-world application experiments demonstrated that randomization of muscle dynamics notably enhanced the control performance of learning-based controllers. Furthermore, our framework exhibited satisfactory performance on both robotic platforms, indicating its great potential of applications in similar systems driven by artificial muscle strings.

Despite the notable performance of the proposed algorithm, several limitations exist. Noticeable jitters in action trajectories may prolong system rise time. Additionally, the configuration of the reward function still has a considerable impact on the experimental outcomes. In future work, we plan to analyze these issues comprehensively using extensive experimental data and refine our algorithms to effectively address these challenges.

REFERENCES

- [1] J. Zhang *et al.*, “Robotic artificial muscles: Current progress and future perspectives,” *IEEE Trans. Robot.*, vol. 35, no. 3, pp. 761–781, 2019.
- [2] S. Y. Yang *et al.*, “Hybrid antagonistic system with coiled shape memory alloy and twisted and coiled polymer actuator for lightweight robotic arm,” *IEEE Robot. Automat. Lett.*, vol. 7, no. 2, pp. 4496–4503, 2022.
- [3] R. J. Wood, “The first takeoff of a biologically inspired at-scale robotic insect,” *IEEE Trans. Robot.*, vol. 24, no. 2, pp. 341–347, 2008.
- [4] Z. Chen, S. Shatara, and X. Tan, “Modeling of biomimetic robotic fish propelled by an ionic polymer–metal composite caudal fin,” *IEEE/ASME Trans. Mechatron.*, vol. 15, no. 3, pp. 448–459, 2009.
- [5] S. Liu, F. Wang, Z. Liu, W. Zhang, Y. Tian, and D. Zhang, “A two-finger soft-robotic gripper with enveloping and pinching grasping modes,” *IEEE/ASME Trans. Mechatron.*, vol. 26, no. 1, pp. 146–155, 2020.
- [6] N. Nikdel, P. Nikdel, M. A. Badamchizadeh, and I. Hassanzadeh, “Using neural network model predictive control for controlling shape memory alloy-based manipulator,” *IEEE Trans. Ind. Electron.*, vol. 61, no. 3, pp. 1394–1401, 2013.
- [7] S. Mao *et al.*, “Gait study and pattern generation of a starfish-like soft robot with flexible rays actuated by smas,” *J. Bionic Eng.*, vol. 11, no. 3, pp. 400–411, 2014.
- [8] D. Hua, X. Liu, S. Sun, M. A. Sotelo, Z. Li, and W. Li, “A magnetorheological fluid-filled soft crawling robot with magnetic actuation,” *IEEE/ASME Trans. Mechatron.*, vol. 25, no. 6, pp. 2700–2710, 2020.
- [9] G. Gerboni, A. Diodato, G. Ciuti, M. Cianchetti, and A. Menciasci, “Feedback control of soft robot actuators via commercial flex bend sensors,” *IEEE/ASME Trans. Mechatron.*, vol. 22, no. 4, pp. 1881–1888, 2017.
- [10] A. Firouzeh, M. Salerno, and J. Paik, “Stiffness control with shape memory polymer in underactuated robotic origamis,” *IEEE Trans. Robot.*, vol. 33, no. 4, pp. 765–777, 2017.
- [11] Y. S. Song and M. Sitti, “Surface-tension-driven biologically inspired water strider robots: Theory and experiments,” *IEEE Trans. Robot.*, vol. 23, no. 3, pp. 578–589, 2007.
- [12] K. H. Cho *et al.*, “A robotic finger driven by twisted and coiled polymer actuator,” in *Proc. SPIE*, 2016, pp. 275–281.
- [13] R. Konda, D. Bombara, E. Chow, and J. Zhang, “Kinematic modeling and open-loop control of a twisted string actuator-driven soft robotic manipulator,” *J. Mech. Robot.*, vol. 16, no. 4, 2024.
- [14] R. Konda, D. Bombara, S. Swanbeck, and J. Zhang, “Anthropomorphic twisted string-actuated soft robotic gripper with tendon-based stiffening,” *IEEE Trans. Robot.*, vol. 39, no. 2, pp. 1178–1195, 2022.
- [15] L. Sutton, H. Moen, A. Rafiee, J. D. Madden, and C. Menon, “Design of an assistive wrist orthosis using conductive nylon actuators,” in *Proc. IEEE Int. Conf. Biomed. Robot. Biomechanics*, 2016, pp. 1074–1079.
- [16] D. Popov, I. Gaponov, and J.-H. Ryu, “Bidirectional elbow exoskeleton based on twisted-string actuators,” in *Proc. IEEE/RSJ Int. Conf. Intell. Robots Syst.*, 2013, pp. 5853–5858.
- [17] J. Ko, M. B. Jun, G. Gilardi, E. Haslam, and E. J. Park, “Fuzzy pwm-pid control of cocontracting antagonistic shape memory alloy muscle pairs in an artificial finger,” *Mechatronics*, vol. 21, no. 7, pp. 1190–1202, 2011.
- [18] M. Giorelli, F. Renda, M. Calisti, A. Arienti, G. Ferri, and C. Laschi, “Neural network and jacobian method for solving the inverse statics of a cable-driven soft arm with nonconstant curvature,” *IEEE Trans. Robot.*, vol. 31, no. 4, pp. 823–834, 2015.
- [19] T. Yang *et al.*, “A soft artificial muscle driven robot with reinforcement learning,” *Sci. Rep.*, vol. 8, no. 1, p. 14518, 2018.
- [20] C. Schlagenhaut *et al.*, “Control of tendon-driven soft foam robot hands,” in *Proc. IEEE-RAS Int. Conf. Humanoid Robots*, 2018, pp. 1–7.
- [21] T. G. Thuruthel, E. Falotico, F. Renda, and C. Laschi, “Model-based reinforcement learning for closed-loop dynamic control of soft robotic manipulators,” *IEEE Trans. Robot.*, vol. 35, no. 1, pp. 124–134, 2018.
- [22] X. You *et al.*, “Model-free control for soft manipulators based on reinforcement learning,” in *Proc. IEEE/RSJ Int. Conf. Intell. Robots Syst.*, 2017, pp. 2909–2915.
- [23] S. K. Rajendran, Q. Wei, N. Yao, and F. Zhang, “Design, implementation, and observer-based output control of a super-coiled polymer-driven two degree-of-freedom robotic eye,” *IEEE Robot. Automat. Lett.*, vol. 8, no. 9, pp. 5958–5965, 2023.
- [24] J. Tao, S. K. Rajendran, Y. Zhang, F. Zhang, Z. Dexin, and T. Shen, “Efficient learning and control of string-type artificial muscle driven robotic systems,” in *Proc. Amer. Control Conf.*, 2024, (Accepted).
- [25] J. I. Kim, M. Hong, K. Lee, D. Kim, Y.-L. Park, and S. Oh, “Learning to walk a tripod mobile robot using nonlinear soft vibration actuators with

- entropy adaptive reinforcement learning,” *IEEE Robot. Automa. Lett.*, vol. 5, no. 2, pp. 2317–2324, 2020.
- [26] S. K. Rajendran and F. Zhang, “Design, modeling, and visual learning-based control of soft robotic fish driven by super-coiled polymers,” *Front. Robot. AI*, vol. 8, p. 809427, 2022.
- [27] J. Zhang, K. Iyer, A. Simeonov, and M. C. Yip, “Modeling and inverse compensation of hysteresis in supercoiled polymer artificial muscles,” *IEEE Robot. Autom. Lett.*, vol. 2, no. 2, pp. 773–780, 2017.
- [28] B. Pawlowski, J. Sun, J. Xu, Y. Liu, and J. Zhao, “Modeling of soft robots actuated by twisted-and-coiled actuators,” *IEEE/ASME Trans. Mechatron.*, vol. 24, no. 1, pp. 5–15, 2018.
- [29] M. C. Yip and G. Niemeyer, “On the control and properties of super-coiled polymer artificial muscles,” *IEEE Trans. Robot.*, vol. 33, no. 3, pp. 689–699, 2017.
- [30] H. Zhang *et al.*, “Design and modeling of a compound twisted and coiled actuator based on spandex fibers and an sma skeleton,” *IEEE Robot. Automat. Lett.*, vol. 7, no. 2, pp. 1439–1446, 2021.
- [31] X. Wang *et al.*, “Deep reinforcement learning: a survey,” *IEEE Trans. Neural Netw. Learn. Syst.*, 2022.
- [32] T. Zhang, R. Tian, H. Yang, C. Wang, J. Sun, S. Zhang, and G. Xie, “From simulation to reality: A learning framework for fish-like robots to perform control tasks,” *IEEE Trans. on Robot.*, vol. 38, no. 6, pp. 3861–3878, 2022.
- [33] T. Luong *et al.*, “Impedance control of a high performance twisted-coiled polymer actuator,” in *Proc. IEEE/RSSJ Int. Conf. Intell. Robots Syst.*, 2018, pp. 8701–8706.
- [34] J. Sun and J. Zhao, “Physics-based modeling of twisted-and-coiled actuators using cosserat rod theory,” *IEEE Trans. Robot.*, vol. 38, no. 2, pp. 779–796, 2021.
- [35] F. Karami, L. Wu, and Y. Tadesse, “Modeling of one-ply and two-ply twisted and coiled polymer artificial muscles,” *IEEE/ASME Trans. Mechatron.*, vol. 26, no. 1, pp. 300–310, 2020.
- [36] S. K. Rajendran, Q. Wei, and F. Zhang, “Two degree-of-freedom robotic eye: design, modeling, and learning-based control in foveation and smooth pursuit,” *Bioinspiration & Biomimetics*, vol. 16, no. 4, p. 046022, 2021.
- [37] C. S. Haines *et al.*, “Artificial muscles from fishing line and sewing thread,” *Science*, vol. 343, no. 6173, pp. 868–872, 2014.
- [38] H. Jiang, C. Xiao, J. Li, Y. Zhong, T. Zhang, and Y. Guan, “Design and modeling of a 2-dof cable-driven parallel wrist mechanism,” in *Proc. IEEE Int. Conf. Robot. Biomimetics*, 2019, pp. 1047–1052.
- [39] T. Haarnoja, A. Zhou, P. Abbeel, and S. Levine, “Soft actor-critic: Off-policy maximum entropy deep reinforcement learning with a stochastic actor,” in *Proc. Int. Conf. Mach. Learn.*, 2018, pp. 1861–1870.
- [40] J. Chung, C. Gulcehre, K. Cho, and Y. Bengio, “Empirical evaluation of gated recurrent neural networks on sequence modeling,” *arXiv:1412.3555*, 2014.
- [41] X. B. Peng, M. Andrychowicz, W. Zaremba, and P. Abbeel, “Sim-to-real transfer of robotic control with dynamics randomization,” in *Proc. IEEE Int. Conf. Robot. Automat.*, 2018, pp. 3803–3810.
- [42] R. Jitsho, T. G. W. Lum, A. Okamura, and K. Liu, “Reinforcement learning enables real-time planning and control of agile maneuvers for soft robot arms,” in *Proc. Conf. Robot Learn.*, 2023, pp. 1131–1153.
- [43] OpenAI *et al.*, “Learning dexterous in-hand manipulation,” *Int. J. Robot. Res.*, vol. 39, no. 1, pp. 3–20, 2020.
- [44] B. Zheng, S. Verma, J. Zhou, I. W. Tsang, and F. Chen, “Imitation learning: Progress, taxonomies and challenges,” *IEEE Trans. Neural Netw. Learn. Syst.*, no. 99, pp. 1–16, 2022.
- [45] K. Wang, H. Zhao, X. Luo, K. Ren, W. Zhang, and D. Li, “Bootstrapped transformer for offline reinforcement learning,” 2022, pp. 34 748–34 761.
- [46] C. Shorten and T. M. Khoshgoftaar, “A survey on image data augmentation for deep learning,” *J. Big Data*, vol. 6, no. 1, pp. 1–48, 2019.
- [47] M. Laskin, K. Lee, A. Stooke, L. Pinto, P. Abbeel, and A. Srinivas, “Reinforcement learning with augmented data,” in *Proc. Adv. Neural Inf. Process. Syst.*, 2020, pp. 19 884–19 895.
- [48] M. Laskin, A. Srinivas, and P. Abbeel, “Curl: Contrastive unsupervised representations for reinforcement learning,” in *Proc. Int. Conf. Mach. Learn.*, 2020, pp. 5639–5650.
- [49] K. Lee, K. Lee, J. Shin, and H. Lee, “Network randomization: A simple technique for generalization in deep reinforcement learning,” *arXiv:1910.05396*, 2019.
- [50] T. P. Lillicrap, J. J. Hunt, A. Pritzel, N. Heess, T. Erez, Y. Tassa, D. Silver, and D. Wierstra, “Continuous control with deep reinforcement learning,” *arXiv preprint arXiv:1509.02971*, 2015.